Journal of Materials Chemistry A

Selective Control of Sharp-Edge Zinc Electrodes with (002) Plane for High-Performance Aqueous Zinc-Ion Batteries

Journal:	*Journal of Materials Chemistry A*
Manuscript ID	TA-ART-02-2024-001013.R1
Article Type:	Paper
Date Submitted by the Author:	21-Mar-2024
Complete List of Authors:	Jeong, Hee Bin; Kookmin University Kim, Dong Il; Kookmin University Yoo, Geun; Gyeongsang National University Dasari, Mohan; Kookmin University, Roy, Arijit; Kookmin University, Materials Science & Engineering Jung, Min; Sungkyunkwan University - Natural Sciences Campus, Jeong, Hyeong Seop; Kookmin University Cha, SeungNam; Sungkyunkwan University, Physics An, Geon-Hyoung ; Gyeongsang National University, Department of Energy Engineering Cha, Pil-Ryung; Kookmin University, Hong, John; Kookmin University, School of Materials Engineering

SCHOLARONE™
Manuscripts

Selective Control of Sharp-Edge Zinc Electrodes with (002) Plane for High-Performance Aqueous Zinc-Ion Batteries

Hee Bin Jeong,[1,†] Dong Il Kim,[1,†] Geun Yoo,[2,†] Dasari Mohan,[1] Arijit Roy,[1] Min Jung,[3] Hyeong Seop Jeong,[1] SeungNam Cha,[3] Geon Hyoung An,[2,*] Pil-Ryung Cha,[1,**] and John Hong[1,***]

[1]School of Materials Science and Engineering, Kookmin University, 77 Jeongneung-ro, Seongbuk-gu, Seoul, 02707, Republic of Korea

[2]Department of Energy System Engineering, Gyeongsang National University, 33 Dongjin-ro, Jinju, Gyeongnam 52828, Republic of Korea

[3]Department of Physics, Sungkyunkwan University, 2066 Seobu-ro, Jangan-gu, Suwon-si, Gyeonggi-do 16419, Republic of Korea

*Correspondence: ghan@gnu.ac.kr

**Correspondence: cprdream@kookmin.ac.kr

***Correspondence: johnhong@kookmin.ac.kr

[†]These authors contributed equally.

Keywords

Zinc anode, dendrite free, etching solution chemical etching, (002) orientation, phase-field modeling

Abstract

The surface properties and stability of the Zn anode are crucial for achieving high-performance aqueous zinc-ion batteries. Here, we applied etching to the Zn metal anode using the highly active H_2SO_5 etching solution to control the exposure level of the Zn (002) crystal plane. Etching for 2 min afforded Zn sharp-edge (ZnSE) structures with the predominant Zn (002) crystal plane on the Zn surface. The Zn (002) crystal plane hindered the growth of protruding Zn dendrites, minimized hydrogen generation, and enabled a high resistance against Zn metal corrosion and the various side reactions with the aqueous electrolyte ions. Consequently, the Zn anode symmetry cells exhibited excellent cyclability (>200 h) at current densities of 3 and 6 mA/cm^2. Furthermore, with the cell configuration of ZnSE||α-MnO_2, the full cells exhibited a high capacitance of 306 mAh/g at a current density of 0.2 A/g, with a good cycle retention of 94% for up to 300 cycles at 0.5 A/g. Our results will help resolve the surface and stability problems afflicting the Zn metal electrode, helping us achieve high-performance AZIBs. Furthermore, 3D phase-field simulations demonstrate the important role of (002) crystal plane orientation during Zn deposition. Specifically, a dendritic protrusion is formed in the film when the (002) plane orientation is normal, whereas a uniform deposition is observed when the (002) plane is parallel to the Zn film.

Introduction

Due to the high demand for portable, high-performance energy-storage systems, liquid-medium-based electrochemical energy-storage systems have been widely employed in futuristic electric vehicles, stationary systems, and portable devices.[1] These systems majorly rely on Li metal and its organic electrolytes. However, since most of the world's Li supply is provided by a few countries, there is the risk of geopolitical and supply chain issues. Although the existing organic electrolytes can guarantee a wide range of operating potential for cells, the decomposed polymer materials present during the charge–discharge process can act as hotspots for thermal runaway in Li batteries, potentially leading to fire disasters.[2,3] Therefore, finding a new metal-based energy-storage system and its corresponding liquid electrolyte is crucial to widening the selection pool and increasing the stability of future energy-storage systems. Aqueous Zn-ion batteries (AZIBs) have attracted significant interest because of the high availability, low cost, and eco-friendly characteristics of Zn.[4–7] Moreover, a water-infused electrolyte solution could serve as an effective barrier, enhancing the overall thermal stability of the system, which can be a promising solution to the problems caused by organic-electrolyte decomposition.[8] However, during the deposition and stripping process, the fast diffusion access of hybridized Zn ions on the Zn metal anode can induce a malfunction in the AZIB operation. During the deposition process, the protruding structure of Zn dendrites on the Zn metal anode can damage the separator and cause a short circuit in the AZIBs.[9,10] The hydrogen generation and the Zn corrosion caused by parasitic surface reactions on the native passivation layers of Zn metal anodes pose additional problems, leading to decreased cycling stability of AZIBs.[11,12] Therefore, finding a strategy for controlling the favorable kinetics between the hybridized Zn ion and the Zn metal anode is crucial to addressing these challenges.

The problems associated with the Zn metal anode can be resolved by controlling its surface properties. This can be achieved by tailoring the surface energy, inducing favorable Zn facets, and coating with heterogeneous nano- and bulk materials.[13] Among these methods, inducing favorable Zn facets holds the most promise for enhancing the overall performance of AZIBs.[14–17] This is because the surface energy is strongly related to the crystal domain of the Zn surface (Zn facets).[18] Moreover, the adsorption and desorption mechanisms can be favorably tuned by coating with heterogeneous materials. However, these materials conventionally require additional surface treatments and complex coating processes for the highly ductile Zn metal, limiting the scalability and production of the electrodes.[19,20] Furthermore, these materials can be peeled off, necessitating the use of adhesion materials that may hinder Zn-ion deposition and stripping in AZIBs. A recent study revealed that, compared with other facets, the Zn (002) crystal plane holds promise for application in suppressing the growth of protruding Zn dendrites. Further, it increases the tolerance of the Zn anode against corrosion and hinders the hydrogen evolution reaction (HER). For example, Zhang et al. reported the introduction of $BMIm^+$ ions, which can be adsorbed and hinder the deposition of Zn ions on the (100) and (101) planes. Therefore, most of the Zn ions were deposited on the (002) plane; this helped control the shape and formation of dendrites as they could grow on the specific (002) plane.[21] Moreover, Zhang et al. fabricated a dense (002)-textured Zn substrate by galvanostatic electrodeposition. This (002)-textured Zn could provide dendrite-free and HER-suppressed Zn electrodes.[22] Therefore, finding an easy and effective method for selectively exposing the (002) crystal plane on the Zn anode is crucial for designing high-performance AZIB metal anodes.

In this paper, we present an ultrafast fabrication strategy (under 5 min) for producing a Zn sharp-edge (ZnSE) electrode with the abundant and favorable (002) crystal plane. This is achieved by a simple solution-based exposure method using a etching solution (H_2SO_5). On the surface of the Zn metal anode, the etching speed of heterogeneous facets can be determined

by its surface energy.[23] Except for the stable Zn (002) crystal plane, most of the other crystal planes (such as 100 and 101) can be easily removed using the highly active etching solution, leaving only the stable (002) facet on the surface with the sharp-edge structures. We further demonstrate that the ZnSE electrode can suppress the growth of piercing Zn dendrites and deliver excellent charge-storage performance. This enhancement is attributed to the selectively etched Zn surface with the abundant and favorable Zn (002) crystal plane. The remarkable surface and morphological properties of ZnSE ensure that the ZnSE||ZnSE symmetrical cells maintain stable electrochemical plating/stripping cycling for over 200 h at both current densities of 3 and 6 mAh/cm^2. In addition, the ZnSE||α-MnO_2 asymmetric cells exhibit a capacitance of 306 mAh/cm^2 at a current density of 0.2 A/g, which is higher than that of the bare Zn foil with a capacitance of 237 mAh/cm^2. The retained cycling capacity was over 94% of the initial value after 300 cycles at a current density of 0.5 A/g. The enlarged (002) facet and surface structure could also minimize the effects of surface corrosion and side reactions, as well as hydrogen generation, which would have otherwise damaged the physical hindrance of the Zn electrodes. To further reveal and understand the relationship between the surface facet and Zn dendrite growth, the morphological evolution and related properties on the Zn electrode due to the developed overpotential of the AZIB are investigated by phase-field modelling. The calculations demonstrate the formation of a stable facet at the (002) plane, as well as a corner connecting to other crystallographic planes. These calculations are based on anisotropic interfacial free energy descriptions for both ZnSE and bare Zn foil. When the smallest, most stable, and least energetic (002) facet is vertically aligned with the hybridized Zn-ion path, it is expected to result in smooth and uniform Zn dendrites. This alignment is similar to the protruding dendrites formed when the (002) facet is positioned at a 90° angle to the Zn-ion path. This observed structure closely matches the dendrite formation of ZnSE during the Zn deposition and stripping processes.

Results and Discussions

A diagram illustrating the preparation process of the ZnSE electrode with the dominant Zn (002) crystal plane using a facile and simple etching process with the etching solution is shown in **Figure 1**. Due to the high etching ability of the etching solution, the Zn foil was immediately etched when it was immersed, subsequently generating hydrogen and Zn ions on the surface of the foil. During the etching process, crystal planes other than the Zn (002) plane reacted immediately. The Zn (002) crystal plane did not react because of its high tolerance. Therefore, the enlarged Zn (002) plane could be maintained stably on the surface of the Zn foil. The subsequent plane-selective etching procedures allowed the fabrication of ZnSE with the abundant Zn (002) crystal plane. The depth and density of the ZnSE, as well as the exposure degree of the (002) crystal plane, were managed by adjusting the etching time (not exceeding 5 min). Finally, the etched Zn foils were cleaned with DI water and ethanol for use as the electrode in AZIBs.

Figure 2A illustrates the exposure level of the Zn (002) crystal plane of the Zn foil after etching with the etching solution. On the bare Zn foil, several crystal planes, including (101), (100), and (002), and the original passivation layers (ZnO) are randomly distributed. After etching with the etching solution for 2 min, other crystal planes and passivation layers were easily etched by the highly active etching solution, whereas the (002) facet, due to its strong interatomic plane bond, remained unaffected. Consequently, the sharp-edge structures with the Zn (002) crystal plane were finally fabricated. The largely exposed (002) plane could ensure stable surface chemistry by hindering hydrogen generation and increasing the anode's tolerance against corrosion, as well as promoting the horizontal electrochemical plating of Zn, thus improving the electrochemical reversibility.[24] The surface microarchitectures of ZnSE were

characterized by scanning electron microscopy (SEM) and atomic force microscopy (AFM), and the results are shown in **Figure 2B**. The surface of the bare Zn foil shows some bulk streaks, which is originated from the Zn merchant fabrication. Also, conventionally, during the Zn merchant fabrication, some passivation layers are introduced on the bare Zn foil. After the chemical etching for 2 min, the initial streak layers became thin. Moreover, the sharp and aligned crystallographic planes of metallic Zn were observed. This implies that the initial surface layers on the pristine Zn foil were removed, and the specific crystallographic orientation of hexagonal metallic Zn was exposed on the surface. Finally, the X-ray diffraction (XRD) patterns of the ZnSE and bare Zn foil were recorded and are shown in **Figure 2C**. For the bare Zn foil, the intensity of the (002) peak is lower than that of the (100) peak. After etching with the concentrated etching solution, the intensity of the (002) peak increased significantly. To understand the effects of the etching time on the bare Zn foil, as shown in **Figure S1**, different etching times were applied, and the uniformity and surface structures of the resulting materials were analyzed. The Zn foils were denoted as follows based on the different etching times: ZnSE-0.5 (for 30 s), ZnSE (for 2 min), and ZnSE-5 (for 5 min). For the etching time of 30 s, the exposure level of the Zn (002) crystal plane was relatively increased; however, the SEM and AFM images **(Figures S1A and S1B)** show that the etching proceeded unevenly because of the insufficient exposure time. For the 5-min etching, the exposure level of the Zn (002) crystal plane was similar to that in the bare Zn foil. The surface turned even, the survived (002) facet was also etched, and the overall thickness of the Zn foil decreased. As shown in **Figure 2C and Figure S1C**, after etching with the concentrated etching solution, the peak intensity ratio (I_{002}/I_{100}) increased from 1.029 for ZnSE-0.5 to 1.14 for ZnSE. However, when the etching time reached 5 min, the corrosion reaction of the Zn (002) crystal plane for ZnSE-5 dominantly occurred, leading to a decrease in the I_{002}/I_{100} ratio to 0.26, which is similar to the ratio for the bare Zn foil. From these results, we can conclude

that under the etching solution, the etching speed of the (002) facet is lower than those of the (100) and (101) facets. This is attributed to the higher atomic coordination, tighter atomic bonds, and lower dissolution tendency of the (002) facet compared with those of the loosely packed crystallographic (100) and (101) facets. The ZnSE-0.5 sample shows not only the Zn (002) crystal plane but also other crystal planes, which remain on the surface of the Zn foil. For the 2-min etching time, the Zn (002) crystal plane survived predominantly, and its exposure level was selectively increased, attributed to its strong interatomic bonds. However, when etching was performed for a relatively long period (i.e., 5 min), the Zn (002) crystal plane was also etched, similar to other crystal planes (**Figure S2**).

Figure S3 displays the coherence scanning interferometry (CSI) profiler images of both the ZnSE and the bare Zn foil. The calculated square root depth (S_q) of ZnSE is approximately 0.221 μm, which is smaller than that of the bare Zn foil (0.263 μm). Sq represents the standard deviation of the average roughness, and it is calculated by considering the + and − height distributions in the Z-axis on the average surface. The formula for calculating Sq is as follows:

$$S_q = \sqrt{\frac{1}{A}\iint_A Z^2(x,y)dxdy} \qquad \text{Eq. (1)}$$

Additionally, the sharp edges are clearly observed in the CSI profiler images, consistent with the SEM and AFM results. For electrochemically homogeneous Zn-ion deposition and stripping, a hydrophilic Zn-anode surface is highly desirable in AZIBs. This can be evaluated by contact angle measurements (CAMs) (**Figure S4**). The ZnSE surface performs much better than that of the bare Zn foil in terms of the contact angle of DI water, where the contact angle on ZnSE is only 11.74°. By contrast, the contact angle of DI water on the surface of the bare Zn foil is stabilized at 89.63°. The superior hydrophilic properties of ZnSE improve the surface accessibility of the Zn anode to aqueous electrolyte ions and, hence, facilitate homogeneous Zn deposition with more uniform electrochemical-ion transport.[25,26] Therefore, according to

the SEM, AFM, XRD, CSI, and CAM results, the abundant Zn (002) crystal plane was selectively exposed with the sharp-edge structures through immersion in the etching solution. Compared to the bare Zn foil, the ZnSE electrode possesses a hierarchically sharp surface structure. Additionally, the largely exposed preferential Zn (002) crystal plane can enhance the cyclability and stability of the Zn metal electrode by increasing its tolerance to HER and corrosion reactions, as well as inhibiting the growth of protruding Zn dendrites.

To better describe the HER and corrosion tolerance of the prepared anodes, a three-electrode system was employed, consisting of the prepared Zn foil anode (working electrode), Pt foil (counter electrode), and Ag/AgCl (reference electrode). Chronoamperometry (CA), as shown in **Figure 3A,** was conducted at an overpotential of −150 mV for 300 s to indirectly demonstrate the nucleation processes of Zn^{2+} ions on the Zn metal surface. Up to 300 s, the current density of the bare Zn foil gradually increased, whereas that of ZnSE gradually stagnated at −16.19 mA/cm^2, indicating the uniform deposition of Zn ions on the ZnSE. The increase in the current density over time suggests the 2D diffusion of Zn ions along the surface of the metal anodes, where the Zn ions laterally migrate to find energetically favorable sites and minimize the surface energy, leading to nonuniform Zn aggregation and dendrite growth. However, the stable and continuous current density can insinuate the uniform 3D diffusion of Zn ions, indicating that the absorbed Zn ions can be directly reduced to metallic Zn without any lateral transfer on the surface. Therefore, ZnSE can provide the 3D diffusion paths for Zn ions, facilitating the uniform deposition of Zn ions on the surface of ZnSE. The electrochemical stability window of the electrolyte was determined through anodic linear sweep voltammetry (LSV) scans, as depicted in **Figure 3B**. The LSV is one of the powerful tool to understand the HER conditions for the as-prepared Zn anode materials.[27-32] HER in acidic conditions is represented by followed chemical reaction formula:

$$2H^+ + 2e^- \rightarrow H_2$$

The ZnSE anode caused shifts in the hydrogen evolution potentials. Specifically, the fact that the hydrogen evolution potential became more negative provides sufficient evidence to support the inhibition of hydrogen generation from ZnSE. The hydrogen evolution potential of ZnSE is more negative than that of bare Zn foil, indicating that ZnSE can effectively reduce the occurrence of side reactions. Under the LSV test conducted at a scan rate of 5 mV/s, the cathodic current density exhibited a rapid increase for the bare Zn foil **(Figure 3B)**. The introduction of a metal with a higher HER overpotential to suppress the HER catalytic activity of the anode has also been proposed. The ZnSE anode possesses higher hydrogen overpotential (−1.75 V vs. Ag/AgCl) than the bare Zn foil (−1.69 V vs. Ag/AgCl), as confirmed by the higher charge efficiency and reduced gas generation. Additionally, the corrosion performance was analyzed by linear polarization measurement in a 2 M $ZnSO_4$ electrolyte. As shown in **Figure S5A**, the corrosive potential of ZnSE (−0.95V) is slightly higher than that of the bare Zn foil (−0.96 V). In addition, the corrosion current density of ZnSE is slightly higher than that of the pristine Zn foil. The slightly increased corrosion rate can be attributed to the increased accessibility of Zn to the electrolyte in ZnSE, reflecting the successful formation of the sharp-edge architecture after the etching on the Zn foil surface.[33] **Figure S5B** shows the corrosion degree of Zn foil after electrochemical charging and discharging, obtained by optical microscopy. For the bare Zn foil, it can be observed that a high degree of corrosion occurs. Fewer side reactions occurred during the charge–discharge processes, owing to the comparatively high free energy of hydrogen adsorption and low loss energy of Zn on the Zn (002) anode surface.[14]

To investigate the electrochemical properties of the ZnSE electrode, ZnSE||ZnSE symmetric cells were assembled using an aqueous 2 M $ZnSO_4$ + 0.2 M $MnSO_4$ electrolyte. As shown in

Figure 3C and Figure S6, the ZnSE electrode exhibited stable electrochemical plating/stripping behavior, with an overpotential of 36.5 mV for 250 h at a current density of 3 mA/cm^2 and an aerial capacity of 1 mAh/cm^2. In contrast, the bare Zn electrode had a much shorter lifespan of 60 h, with a significantly higher overpotential of 55.5 mV under the same conditions. These results demonstrated the enhanced electrochemical performance of the ZnSE electrode, with an increase in the number of electrochemical active sites. The low overpotential of the ZnSE electrodes reflected the rapid ion transport at the electrode/electrolyte interface, which could also be attributed to the clean surface and sharp Zn edge structure of the electrode.[34] As illustrated in **Figures S7A and S7B**, the electrochemical stability of the ZnSE||ZnSE symmetrical cells was established at a fast-current density of 6 mA/cm^2 with areal capacities of 1 mAh/cm^2 and 10 mAh/cm^2, respectively. The ZnSE||ZnSE symmetrical cells maintained stable electrochemical plating/stripping cycling for 200 h at a current density of 6 mA/cm^2 and an aerial capacity of 1 mAh/cm^2, In comparison, the bare Zn||Zn symmetrical cells failed after 77 h under the same test conditions, further demonstrating the vital role of the clean surface and sharp-edge structure in improving the electrochemical cycling stability of the Zn electrode. For this stability test, the ZnSE derived from a Zn foil with a thickness of 50 μm was utilized to physically withstand the high areal capacitance condition. The XRD patterns of ZnSE further revealed that the etching method preferentially activates the (002) crystal plane over the (100) crystal plane, a finding consistent with the results obtained from the ZnSE derived from the Zn foil of 25 μm thickness (**Figure S8**). Under these electrochemical conditions, the ZnSE||ZnSE symmetrical cells showed the high cycling stability, exhibiting a stable overvoltage in comparison to the symmetrical cells with the bare Zn electrodes. **Figure S7C** also shows the voltage profile of the ZnSE at the current density of 3 mA/cm^2 and the capacity of 2 mAh/cm^2 for the comparison. The polarization voltage profiles of the ZnSE according to the etching time at various current densities are shown in **Figure S7D**. The rate

test revealed that the ZnSE symmetric cell had a considerably lower voltage hysteresis than the bare Zn cell. In the rate-performance test at 0.1 mA/cm^2, the bare cell exhibited different overvoltage variations over time, whereas the ZnSE displayed a constant overvoltage pattern. These results indicate that the shape of the overvoltage varies from cycle to cycle, due to the nonuniform passivation layer on the bare Zn foil. Such improvements could be attributed to the removal of the surface passivation layer and the enlargement of the electrochemically active area for the ZnSE electrode. After the 5th cycle, the overpotential of the bare Zn electrode decreased to 35 mV, and the electrode was activated. The passivation layer on the bare Zn electrode was detrimental to the electrochemical plating/stripping, consequently reducing electrical conductivity and limiting the diffusion of Zn ions. For the ZnSE electrode, the overpotential was ~15 mV at the 5th cycle, which was nearly the same as the overpotential value at the 1st cycle (~22 mV), highlighting the improved kinetics of the plating/stripping behavior of ZnSE. **Figure S7E** shows the voltage profile of the ZnSE symmetric cell cycled under 20% depth of discharge (DOD) at a current density of 6 mA/cm^2 and an aerial capacity of 3 mAh/cm^2, demonstrating the excellent cycling stability with the voltage hysteresis of 40 mV. In contrast, the bare Zn foil symmetric cell exhibits large overpotential only after 40 h under the same testing condition. The ZnSE symmetric cell voltage profile was also analyzed under 40% DOD at a current density of 6 mA/cm^2 and at an aerial capacity 6 mAh/cm^2 at 6 mA/cm^2 and 6 mAh/cm^2 (**Figure S7F**). The voltage profile also shows that the ZnSE symmetric cell can be stably cycled for ~70 h with no signs of short circuit, while the bare Zn foil symmetric cell exhibits high voltage hysteresis and becomes short-circuited. Moreover, the SEM images of the cycled ZnSE and bare Zn foil with a low magnitude are shown in **Figures S7G and S7H.** The piercing and low-density Zn dendrites can be detected on the bare Zn foil, although the uniform and smooth deposition of Zn on the ZnSE electrode can be confirmed. In terms of the overpotential, etching time and electrochemical performance, the ZnSE electrode

is superior to many of the recently reported etched Zn electrodes (**Table S1 and Table S2**).

To study the morphology and surface hindrance of ZnSE, the ZnSE and bare Zn electrodes were electrochemically swept for 60 cycles at a current density of 6 mA/cm^2, with a set capacity of 1 mAh/cm^2 for the electrochemical dendrite test. Additionally, to explore the side reactions between the Zn anode and the electrolyte, the samples were soaked in 2 M $ZnSO_4$ for 7 days (the by-product test against the corrosion reactions). The homogeneous and hexagonal Zn (002) planes can be explicitly visualized on ZnSE, according to the SEM images with a high magnitude (**Figure 4A**) after the electrochemical dendrite test. Conversely, on the bare Zn foil, the protruding Zn dendrites can be easily detected. Furthermore, the morphology difference between the ZnSE and bare Zn foil after the by-product test was confirmed. On the bare Zn foil, the surface was etched and corroded by the electrolyte ions, exhibiting various nanostructures. However, the ZnSE electrode could well maintain its original planar structure (**Figure 4B**). **Figure 4C** shows the CSI profile images of the ZnSE and bare Zn foil after the electrochemical dendrite test. The S_q value of ZnSE is considerably smaller than that of the Zn bare foil, indicating the uniform deposition and planar growth of Zn on the surface of ZnSE. Finally, the XRD patterns of the ZnSE and the bare Zn foil are shown in **Figure 4D and Figure S9,** obtained after the electrochemical dendrite test and by-product test. Several new peaks, clearly located at 9.5°, 19.1°, and 28.9°, emerged after the side reactions of the Zn foil with electrolyte, corresponding to the (002), (004), and (006) planes of $Zn_4SO_4(OH)_6{\cdot}3H_2O$ (PDF.#04-012-8190), respectively. After both tests, the peak intensity of the (002) plane for the ZnSE electrode was larger than that of the (100) plane, indicating the surface anisotropy with the large exposure level of the (002) plane. Moreover, a larger amount of the by-products ($Zn_4SO_4(OH)_6{\cdot}3H_2O$) is observed on the bare Zn foil than on the ZnSE electrode. The SEM and XRD results after the electrochemical dendrite and by-product test can be attributed to the selectively and largely exposed (002) planes after the etching process. On the ZnSE electrode,

the Zn ions tend to deposit on the surface of the electrode along the horizontal direction, guiding the preferential orientation of the Zn crystal growth sequentially parallel to the sheet's surface. However, the crystallographic direction of the bare Zn foil is randomly distributed along other planes, creating protruding and spongy-like Zn dendrites.[35] **Figure S10** illustrates the important role of ZnSE in improving the electrochemical plating/stripping behavior. A native nonuniform passivation layer generally exists on bare metallic Zn foil because of its high chemical reactivity. Such a passivation layer mainly consists of ZnO and other Zn-containing species, which can lead to high and nonuniform surface electrochemical impedance.[36] Further, the nonuniform local surface structure leads to nonuniform Zn plating/stripping and, eventually, by-product formation. In our experiment, the introduced chemical polishing process could remove the nonuniform surface passivation layers, leaving a clean surface of metallic Zn with a uniform sharp-edge structure. The clean surface and its unique ZnSE morphology can reduce the nucleation overpotential (**Figure S11)**, facilitated by the highly uniform and relatively low electric-field requirement for deposition and stripping on the ZnSE surface. **Figure S12** also shows the columbic efficiencies of the asymmetric cells at different current densities and areal capacitance, indicating the significantly improved reversibility of the ZnSE.

Inspired by the outstanding plating/stripping performance, the full cells with the configuration of ZnSE||α-MnO_2 were assembled to assess the AZIB performance. In this work, the as-synthesized α-MnO_2 exhibits a needle-like morphology with high purity (**Figure S13)**. With the cathode kept fixed, higher capacity, better cycling stability, and higher rate capability are achieved using ZnSE compared with the results achieved using the bare Zn foil anode. The rate capabilities of the full cells with ZnSE-0.5, ZnSE, ZnSE-5, and the Zn foil are presented in **Figure 5A**. The specific capacity of ZnSE||α-MnO_2 is higher than that of the bare Zn||α-MnO_2 at different current densities. The GCD profile of the ZnSE at different current density (0.1–5.0 A/g) are shown in **Figure S14**. The cycling stability of two full batteries was examined by

galvanostatic charge–discharge measurements at a current density of 0.5 A/g **(Figure 5B)**. During the 300 cycles, the ZnSE||α-MnO_2 cell exhibited a capacitance retention of 94%, which is better than that exhibited by the bare Zn||α-MnO_2 (44%). As shown in **Figure S15**, the capacitance retention from the initial up to the 15th to 30th cycles for the ZnSE||α-MnO2 full cell at low current densities of 0.2 A/g and 0.05 A/g is well preserved in comparison to that of the bare Zn foil, denoting its high endurance resistance. Electrochemical impedance spectroscopy (EIS) was carried out to study the charge transfer on full cells using the ZnSE and the bare Zn foil. As shown in **Figure 5C**, the charge-transfer resistance of the ZnSE electrode after cycling was ~17 Ω, much lower than that of the bare Zn electrode (~48 Ω). This demonstrates the important roles of the fresh electrode surface and the ZnSE structure. As shown in **Figure 5D**, the peak intensity ratio ($I_{(002)}/I_{(100)}$) of ZnSE is higher than that of the bare Zn foil after the cycling, revealing that the ZnSE and its selectively exposed (002) crystal plane can induce the preferred crystal orientation of Zn during the Zn plating and stripping. The cycled ZnSE electrode exhibits a higher $I_{(002)}/I_{(100)}$ value (1.56) than the ZnSE-0.5 (0.96) and ZnSE-5 (0.8) electrodes, indicating the largely selective nucleation along with the (002) crystal plane. These above results reveal the improved reaction kinetics and stability of the ZnSE electrode, attributed to the removal of the surface passivation layer and the construction of the ZnSE. The typical CV curves of the as-assembled aqueous full cells are shown in **Figure S16**. Notably, the ZnSE||α-MnO_2 full cell exhibits a higher current density and smaller anodic/cathodic gap than the bare Zn foil||α-MnO_2. This information indicates that the ZnSE electrode improves the specific capacity and charge-transfer kinetics. The action mechanism of the ZnSE is similar to that of the bare Zn foil electrode, but the difference lies in the Zn deposition/stripping location. As shown in **Figure 5E,** on the pristine Zn foil, the Zn ions are deposited randomly in locations where a high electrical field can be applied to the Zn surface. Therefore, continuous Zn deposition/stripping can introduce nonuniform and protruding Zn

dendrites. However, within the structure of ZnSE, the peak node of the sharp-edge structure is aligned with the (002) plane, where the activity with Zn ions is lower than those for other planes. Consequently, most Zn ions are deposited and stripped in the channels between the Zn sharp edges, which are beneficial for the uniform flux of Zn ions. These can also inhibit the growth of protruding Zn dendrites, resulting in uniform Zn deposition/stripping. Moreover, the special structure of the as-synthesized ZnSE with the predominant (002) crystal plane endows high-performance AZIBs with excellent cycling stability. In summary, after the etching treatment, the unique ZnSE structures and largely exposed Zn (002) crystal plane were beneficial for the stability of AZIBs. The ZnSE electrodes exhibit improved the anticorrosion ability of the anode and minimized hydrogen generation. This result is due to the low local current density of the ZnSE, as well as the high hydrogen adsorption free energy and strong chemical bonds of the (002) plane.[14] Additionally, the predominant (002) crystal plane, with its comparatively strong atomic packing density and adsorption energy with Zn, induces parallel deposition on the basal (002) plane and sustains the horizontal growth of the Zn (002) surface. As shown in **Table S3**, it has been noted that the (0001) plane exhibits the minimum energy among all crystal planes of Zn. In single-phase alloys, the etching response varies for each plane; thus, surfaces with higher energy may react to the etchant more actively due to the surface energy interaction. The (0001) plane, possessing lower energy, is consequently less etched compared to planes with higher surface energy of Zn. The rate of etching in any process is predominantly determined by the duration of etching and activity of etching precursors. In the experiments, the activity of the etching precursors was carefully controlled, with the etching time being the only variable to systematically control the surface of Zn.

To validate experimental observations, computer modeling through phase-field simulations[37-39] are conducted on a simulation domain measuring $3.2 \times 12.8 \times 12.8\ \mu m^3$ ($64 \times 256 \times 256$ grid points). The phenomenological interface width was set at 10 grid points, and the initial size of

the metallic phase was modeled as a sphere with a radius of 5 grid points (above the critical size of the metallic Zn nucleus owing to electrolyte supersaturation with the Zn ions set at 0.51). Owing to computational constraints, the simulation domain represented a section view of the battery (focusing on the anode and electrolyte enriched with Zn cations). To ensure a continuous supply of cations, a Dirichlet boundary condition was applied at the right boundary (mimicking the anode) with a value of 0.45. An external potential, mimicking the battery overpotential, was applied to the Zn working electrode at −0.01 V, while the counter electrode remained unbiased at 0. The electric field drove the Zn^{2+} ion toward the low biasing voltage direction, directed toward the Zn electrode. The morphological evolution of the metallic Zn electrode phase for various crystallographic orientations relative to the working electrode is presented in **Figure 6** (represented as phase-field iso-surface drawn at $\varphi = 0.5$). All results were synchronized at the same time (34 ms) across different conditions. After the phase-field calculation, Top and side views of Zn electrodes with the different crystal planes are represented in **Figures 6A and 6B** for understanding the 3D growth morphologies for two different choices of θ, 0° and 90°, respectively. In **Figure 6A**, where θ = 0° and the (002) plane was normal to the reference X-axis, a planar growth with in-plane hexagonal symmetry was observed in the top view. From the side view, growth along the [002] direction appeared smaller compared with the in-plane growth. **Figure 6B** represents Zn deposition for θ = 90°, with the [002] direction perpendicular to the external X-axis. Herein, deposition along the X-direction was more extensive than in the θ = 0° condition. The increased Zn deposition for θ = 90° accelerated the possibility of a faster short circuit compared to θ = 0°. This anisotropic growth of Zn deposition led to diverse morphologies for different orientations. In the case of etched ZnSE and bare Zn foil, only (002) planes and multiple orientations were observed. Notably, the simulation results align with the experimental findings for bare Zn foil and etched ZnSE microstructures. **Figure 6C** represents the calculated current density for the applied

overpotential. For θ = 90°, the current density continuously decreased as the deposition increased toward the counter electrode. Conversely, for θ = 0°, the current density remained steady, indicating enhanced battery performance. The results shown in **Figure 6C** aligned precisely with the CA results presented in **Figure 3A**, emphasizing the credibility of our modeling calculations and highlighting the excellent electrochemical performance of ZnSE for AZIBs.

For detailed cross-sectional and orientation-related calculations, color maps of phase-field, composition, and electric potential were plotted at the mid-plane of the simulation domain along the Z-axis in **Figure S17A** for θ = 0° and **Figure S17B** for θ = 90°. The region with φ = 1 represented the metallic Zn phase on the working electrode, while φ = 0 represents the electrolyte. The region with $0 < \varphi < 1$ represents the interface region. A gradual change in Zn ion composition was observed when moving away from the electrode. **Figure S18** represents the growth of Zn as a function of θ, revealing an increased deposition with a high θ angle and suggesting that Zn (002) planes are more favorable for stable electrode configuration when they are aligned parallel to the Zn working electrode. Finally, we implemented the growth of two crystals with different orientations using a phase-field model.[40] Simulations were conducted with two initial Zn seeds of different orientations, θ = 0° and θ = 90°. **Figure S19** represents the phase-field order parameter iso-surface at 0.5 for Zn deposition conditions with the two orientations θ = 0° and θ = 90°. The combination of seeds with different orientations could mimic the conditions of a bare Zn foil. In the side view image, the deposition extent was high for θ = 90° compared with θ = 0, indicating the dominance of growth on the electrode for the θ = 90° condition. For uniform Zn deposition, θ = 0° is preferred, as observed in the case of ZnSE.

Conclusions

This work demonstrates that simple etching using the highly active etching solution (H_2SO_5) can significantly expose the (002) plane on the Zn metal, which is advantageous for the electrochemical activity of AZIBs. The predominant (002) plane on the Zn metal surface suppresses the growth of protruding Zn dendrites, reduces hydrogen generation, and ensures a high corrosion resistance. Consequently, symmetry cells with this Zn anode exhibit excellent electrochemical stability, rate performance, and capacitive behavior. Furthermore, according to phase-field modeling simulations, the deposited Zn ions on the extensively exposed (002) plane induce much smoother and more planar Zn dendrites, which align well with the experimental results of ZnSE after the electrochemical dendrite test. Our findings illustrate that employing a plane-selective etching process, specifically targeting the stable (002) facets, in combination with a specially formulated highly active etching solution, is a straightforward and viable approach for addressing the challenges of poor surface quality and stability associated with Zn metal electrodes, enabling the achievement of high-performance AZIBs.

Material and Methods

Preparation of the Zn Sharp Edge

The ZnSE was fabricated using commercial Zn foil (purity: 99.95^{+}%, thickness: 0.025 mm, 0.05 mm) as the starting material by chemical etching. Typically, a cleaned, bare Zn foil was immersed in a highly active etching solution (H_2SO_5) for 2 min, followed by washing with deionized (DI) water and ethanol. The temperature of the etching solution was maintained at 110°C to ensure uniform control over the etching process. To avoid oxidation, the Zn foil, after etching and rinsing, was dried by Ar blowing.

Synthesis of MnO_2 Nanorods

In a typical synthesis of α-MnO_2, 2.028g of $MnSO_4$□H_2O and 13.2 mL of 3 wt% H_2SO_4 were added to 240 mL of DI water was magnetically stirred until a clear solution was obtained. Thereafter, solution of 1.2642 g of $KMnO_4$ and 40 mL of DI water was slowly added to the above solution. The mixture was stirred for 40 min at room temperature. Subsequently, the solution was transferred to a Teflon-lined autoclave and heated at 120°C for 10 h. The obtained material was collected by filtering, washed with water, and dried using a vacuum oven at 100°C.

Characterization

The phase of the samples was analyzed by XRD (Ultima IV) with Cu Kα radiation. The diffraction patterns were recorded in the 2θ range of 10°–80°. The micromorphologies of the materials and electrodes were observed by SEM (JSM-7401F) with energy-dispersive X-ray spectroscopy (EDX). The morphology of the Zn anode surface was uncovered by AFM (NX10-

AFM) and CSI (Zygo NexView NX2).

Assembly of Symmetric Cells

CR2032-type coin cells were assembled. Zn-foil electrodes were utilized, and an aqueous solution of 2 M $ZnSO_4$ + 0.2 M $MnSO_4$ was employed as the electrolyte. Glass fiber membranes with a diameter of 19 Φ served as separators.

Assembly of Asymmetric Cells

CR2032-type coin cells were assembled. Zn-foil electrodes and Cu-foil electrodes were utilized, and an aqueous solution of 2 M $ZnSO_4$ was employed as the electrolyte. Glass fiber membranes with a diameter of 19 Φ served as separators.

Assembly of Zinc-Ion Battery Full Cells

Coin cells (2032-type) were assembled. ZnSE and the bare Zn foil (Φ = 13 mm) were separately matched with α-MnO_2 nanosheet cathodes. The electrolyte used was an aqueous solution of 3 M $ZnSO_4$ + 0.3 M $MnSO_4$. Glass fiber membranes (Φ = 19 mm) were used as separators. The cells were sealed in air and left for 1 h before electrochemical tests.

Electrochemical Measurements

The ZnSE and bare Zn foil were first cut into disks (Φ = 13 mm) and used as electrodes for electrochemical characterizations. The bare Zn||Zn and ZnSE||ZnSE symmetrical cells were assembled with a coin-cell configuration (2032-type) under ambient conditions. The bare

Zn||Cu and ZnSE||Cu asymmetrical cells were assembled with 25 μm cu foil. Glass fiber (Φ = 19 mm) and 3 M $ZnSO_4$ + 0.3 M $MnSO_4$ were used as the separator and aqueous electrolyte, respectively. Electrochemical plating/stripping measurement of the metallic Zn was performed on a Sinopro battery tester (SINOPROMRX Co., Ltd.) at current densities of 3 and 6 mA/cm^2 with a capacity of 1,2,3,6 and 10 mAh/cm^2. EIS was conducted on a Biologic VMP3 electrochemical workstation in a frequency range of 100 kHz to 0.01 Hz, with an AC voltage of 5 mV.

Phase-field model formulation

We implement the phase-field model developed by Roy and Cha[37–39] (hereafter referred as the RC-PFM) to study the effect of the substrate orientation imposed by the choices of ZnSE or bare Zn foil. The details of the phase-field model and implementation are available at Roy *et al.*[37–39] The phase-field order parameter φ is used to represent the metallic Zn eletcrode (β-phase) with $\varphi = 1$ and $\varphi = 0$ for electrolyte (α-phase). At electrode/electrolyte interface, φ varies smoothly between 1 and 0. The composition of Zn^{2+} ion in the electrolyte is written as $C_{M^+}^{\alpha}$ and the composition of the metallic Zn-phase at the working electrode is represented as C_M^{β}. Next, we describe the core of the phase-field model, which is the free energy functional, consisting of a function of chemical concentration field (function of special coordinates), structural function (function of phase-fields), and electrical function (electrostatic energy as a function of potential field).

Such a free energy functional per unit volume of a system can be expressed as follows,

$$F = \int_V \left(f_{bulk}(C_{M^+}^{\alpha}, C_M^{\beta}, \varphi) + \frac{\kappa_\varphi^2}{2}|\nabla\varphi|^2 + \frac{1}{2}\rho\Phi \right) dV \qquad \text{Eq. (2)}$$

f_{bulk} is the bulk free energy per unit molar volume, κ_φ is gradient energy coefficient, $\frac{1}{2}\rho\Phi$ is the expression for the electrostatic energy, composed of ρ as the concentration of electric

charge and Φ as the applied external electric potential. Here f_{bulk} in Eq. (2) is bulk free energy per unit molar volume and is given by the Model-C of Hohenberg and Halperin nomenclature.[41]

$$f_{bulk} = [1-p(\varphi)]f^{\alpha}\left(C^{\alpha}_{M^+}\right) + p(\varphi)f^{\beta}\left(C^{\beta}_{M}\right) + Wg(\varphi) \qquad \text{Eq. (3)}$$

$p(\varphi) = \varphi^3(10-15\varphi+6\varphi^2)$ is the Wang interpolation function.[42] $f^{\alpha}\left(C^{\alpha}_{M^+}\right)$ and $f^{\beta}\left(C^{\beta}_{M}\right)$ are the bulk free energies of α and β phases, respectively. $g(\varphi) = \varphi^2(1-\varphi)^2$ is the double-well potential for α and β phases and W is the double well potential barrier height. At this point

we want to note that we have assumed that the electrode/electrolyte interface is a mixture of the corresponding concentrations and are different from each other, as proposed by Kim-Kim-Suzuki (KKS).[43] The constraint pose by equal diffusion potential (EDP) condition is also implemented in the model. Following are the constraint for concentration-mix and EDP condition,

$$C = [1-p(\varphi)]C^{\alpha}_{M^+} + p(\varphi)C^{\beta}_{M} \qquad \text{Eq. (4)}$$

$$\frac{\partial f^{\alpha}\left(C^{\alpha}_{M^+}\right)}{\partial C^{\alpha}_{M^+}} = \frac{\partial f^{\beta}\left(C^{\beta}_{M}\right)}{\partial C^{\beta}_{M}} \qquad \text{Eq. (5)}$$

The temporal evolution equation for the phase-field can be obtained by considering the variation of F (in Eq. (2)) with respect to φ as follows,

$$\frac{\partial \varphi}{\partial t} = M_{\varphi}\left[\nabla^2_a\varphi - W\frac{dg(\varphi)}{d\varphi} + \frac{dp(\varphi)}{d\varphi}\frac{RT}{V_m}\left(f^{\alpha}_{C_{M^+}} - f^{\beta}_{C_M} - \frac{\partial f^{\alpha}\left(C^{\alpha}_{M^+}\right)}{\partial C_{M^+}}[C_{M^+} - C_M]\right)\right] \qquad \text{Eq. (6)}$$

$\nabla^2_a\varphi$ is anisotropic 3D Laplacian is given by[44]

$$\nabla^2_a\varphi = \nabla\left(\kappa^2_{\varphi}\nabla\varphi\right) + \frac{\partial}{\partial x}\left(|\nabla\varphi|^2\kappa_{\varphi}\frac{\partial\kappa_{\varphi}}{\partial\left(\frac{\partial\varphi}{\partial x}\right)}\right) + \frac{\partial}{\partial y}\left(|\nabla\varphi|^2\kappa_{\varphi}\frac{\partial\kappa_{\varphi}}{\partial\left(\frac{\partial\varphi}{\partial y}\right)}\right) + \frac{\partial}{\partial z}\left(|\nabla\varphi|^2\kappa_{\varphi}\frac{\partial\kappa_{\varphi}}{\partial\left(\frac{\partial\varphi}{\partial z}\right)}\right) \qquad \text{Eq. (7)}$$

M_{φ} is the phase-field mobility, R is the universal gas constant, T (= 300 K) is temperature, and V_m (= 9.16×10^{-6} m^3/mol)[45] is molar volume. The relation between the interfacial energy (σ), gradient energy coefficient (κ_{φ}), phase-field interface with (2λ) and double well barrier height

(W) are given from KKS model[43] as $2\lambda = \frac{\kappa_\varphi}{\sqrt{2W}}\alpha$ and $\sigma = \frac{\kappa_\varphi\sqrt{W}}{3\sqrt{2}}$.

Anisotropy is introduced in phase-field evolution equation through interfacial energy, $\sigma = \sigma_0[1 + \delta_\sigma f_\sigma(\hat{\eta})]$ and phase-field mobility, $M_\varphi = M_{\varphi_0}[1 + \delta_m f_m(\hat{\eta})]$. σ_0 (= 0.5 J/m^2)[46] is isotropic interfacial energy. δ_σ (= 0.0257) and δ_m (= 0.025) are strength of capillary anisotropy and mobility anisotropy, respectively. Isotropic phase-field mobility calculated as, $M_{\varphi_0} = \frac{W}{3\kappa_\varphi^2 a_2 \xi}$ and $\xi = (C_{M^+} - C_M)^2 \frac{\partial^2 f^\alpha(C^\alpha_{M^+})}{\partial C^{\alpha 2}_{M^+}} / D^\alpha$. $\hat{\eta}$ is the unit vector and can be written as $\frac{\nabla\varphi}{|\nabla\varphi|}$.

Six-fold anisotropic function is used to represent the hexagonal anisotropy of the Zn crystal system.[47]

$$f_{\sigma/m}(\hat{\eta}) = \eta_x^6 - 15\eta_x^4\eta_y^2 + 15\eta_x^2\eta_y^4 - \eta_y^6 + p_1\eta_z^4 + p_2\eta_z^2 + p_3\eta_z^6 \qquad \text{Eq. (8)}$$

with p_1 = -3.0, p_2 = 0.0, and p_3 = -10.0. The 3D polar plot of anisotropy function is represented in **Figure S20**. **Figure S20A** represents the view from an arbitrary angle and **Figure S20B** represents the view from Z-direction. We can observe the 6-fold symmetry in XY-plane and the anisotropy takes maximum values in XY-plane along the hexagonal directions and minimum values along Z-direction.

Orientation of dendrite with respect to external coordinate system is introduced through rotation matrix as follows[48]

$$\begin{Bmatrix} \frac{\partial\varphi}{\partial\tilde{x}} \\ \frac{\partial\varphi}{\partial\tilde{y}} \\ \frac{\partial\varphi}{\partial\tilde{z}} \end{Bmatrix} = \begin{bmatrix} 1 & 0 & 0 \\ 0 & \cos\theta_x & -\sin\theta_x \\ 0 & \sin\theta_x & \cos\theta_x \end{bmatrix} \begin{bmatrix} \cos\theta_y & 0 & \sin\theta_y \\ 0 & 1 & 0 \\ -\sin\theta_y & 0 & \cos\theta_y \end{bmatrix} \begin{bmatrix} \cos\theta_z & -\sin\theta_z & 0 \\ \sin\theta_z & \cos\theta_z & 0 \\ 0 & 0 & 1 \end{bmatrix} \begin{Bmatrix} \frac{\partial\varphi}{\partial x} \\ \frac{\partial\varphi}{\partial y} \\ \frac{\partial\varphi}{\partial z} \end{Bmatrix} \quad \text{Eq. (9)}$$

The notations with tilde represent the values in rotated coordinate system. θ_x, θ_y and θ_z represents rotation about X-, Y- and Z-axis, respectively. The evolution of composition is governed by the diffusion flux equation,

$$\frac{\partial C_{M^+}}{\partial t} = \nabla\left[\frac{D(\varphi)}{f_{cc}}\nabla\left(f^{\beta}_{C_{M^+}} + \frac{z_{M^+}F\Phi}{2V_m}\right)\right] \quad \text{Eq. (10)}$$

$D(\varphi)$ is diffusivity of Zn cations ($D(\varphi) = [1 - p(\varphi)]D^{\alpha} + p(\varphi)D^{\beta}$). D^{α} (= 3.68×10^{-10} m^2/s)[46] and (D^{β} = 3.68×10^{-20} m^2/s) are diffusivities of Zn ions inside electrolyte and Zn in electrode, respectively. z_{M^+} is the valence of Zn ion and F being the Faraday constant.

The distribution of the electric potential is obtained by solving the following charge conservation equation,

$$\nabla \cdot [\varsigma(\varphi)\nabla\Phi] = 0 \quad \text{Eq. (11)}$$

$\varsigma(\varphi)$ is the electric conductivity ($\varsigma(\varphi) = [1 - p(\varphi)]\varsigma^{\alpha} + p(\varphi)\varsigma^{\beta}$). ς^{α} (= 0.1 S/m)[45] and (ς^{β} = 1.0×10^{7} S/m)[46] are electric conductivities of electrolyte and electrode, respectively.

Numerical implementation

Phase-field evolution and composition evolution equations are solved using second order accurate finite difference scheme. Gauss-Seidel method is employed to solve the electric potential distribution. Sixth order Lagrange interpolation formula is used for interpolation of phase-field dependent diffusivity and conductivity at mid-points. The external potential applied after the initial seed is stabilized. The schematic of simulation domain is represented in **Figure S21A**. In the simulation's domain, left boundary represents the Zn working electrode. Periodic boundary condition is applied for top and bottom, front, and back boundaries (in a 3-D simulation domain). The right boundary represents the counter electrode. To mimic the developed battery overpotential, the working electrode (left simulation boundary) is set a constant bias with a negative polarity and the counter electrode (right simulation boundary) is maintained at ground. Dirichlet boundary condition is applied at right boundary for a cation composition of 0.45. The orientation of crystal is chosen by rotation of crystal about external axes as shown in **Figure S21B**. 3D orientation of crystal is achieved by selecting finite values

of θ_x, θ_y and θ_z. We define angle between the external reference X-axis and [002] direction as θ. The 3D phase-field simulations are computationally expensive, so GPU is employed for simulations. The evolution equations are implemented in CUDA-C and NVIDIA® A100 GPU is used for simulations.

Acknowledgements

This research was supported by the National Research Foundation of Korea (NRF) funded by the Korea government (MSIT) [No. Grant-1711196809, RS-2023-00244790], [No. Grant-2021M3H4A6A01045764] & [No. Grant-2020M3A7C2114666]. This research is based upon work supported by the Air Force Office of Scientific Research under award [No. FA2386-22-1-4040].

Conflict of Interest

The authors declare no competing interests.

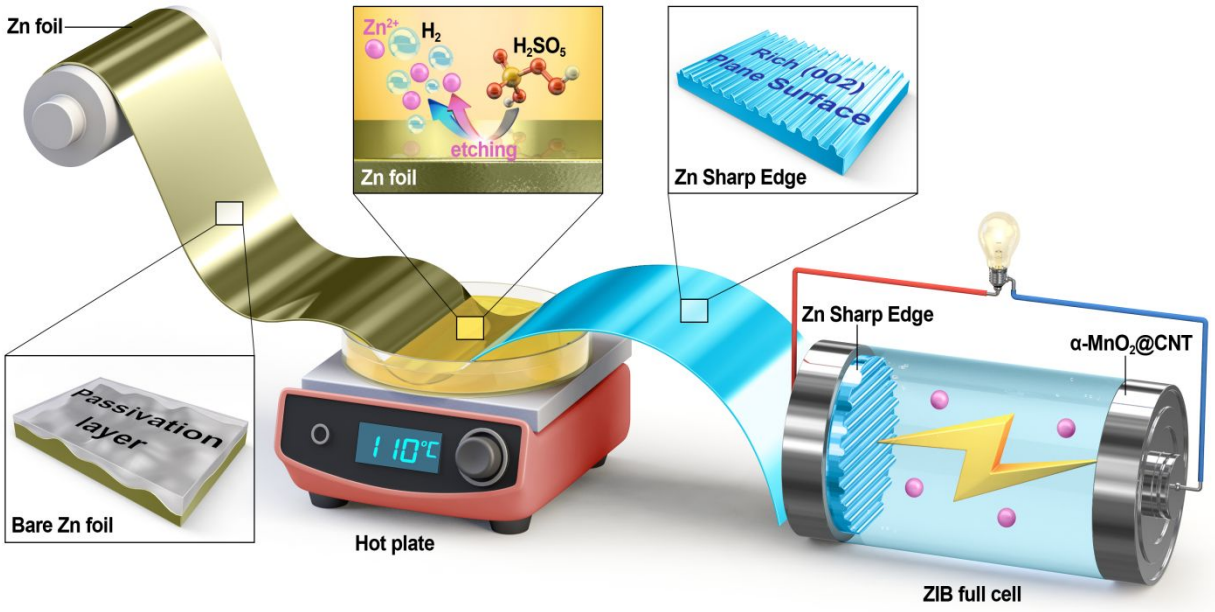

Figure 1. Diagram illustrating the preparation process of the ZnSE electrode.

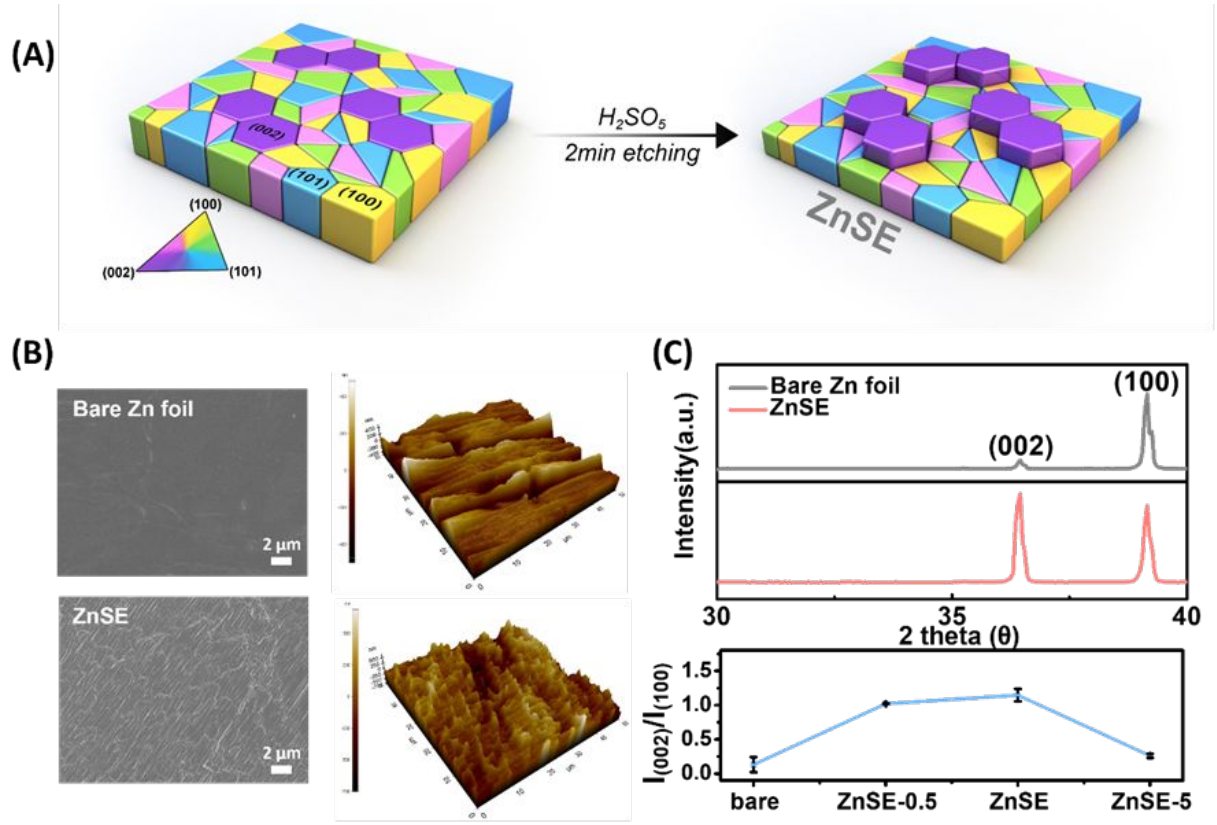

Figure 2. (A) Schematic illustration of the ZnSE formation. (B) Surface SEM and 3D-AFM images of the bare Zn foil and ZnSE. (C) XRD patterns of the bare Zn foil and ZnSE (the inset image shows the peak intensity ratios ($I_{(002)}/I_{(100)}$) of the bare Zn foil and ZnSE.

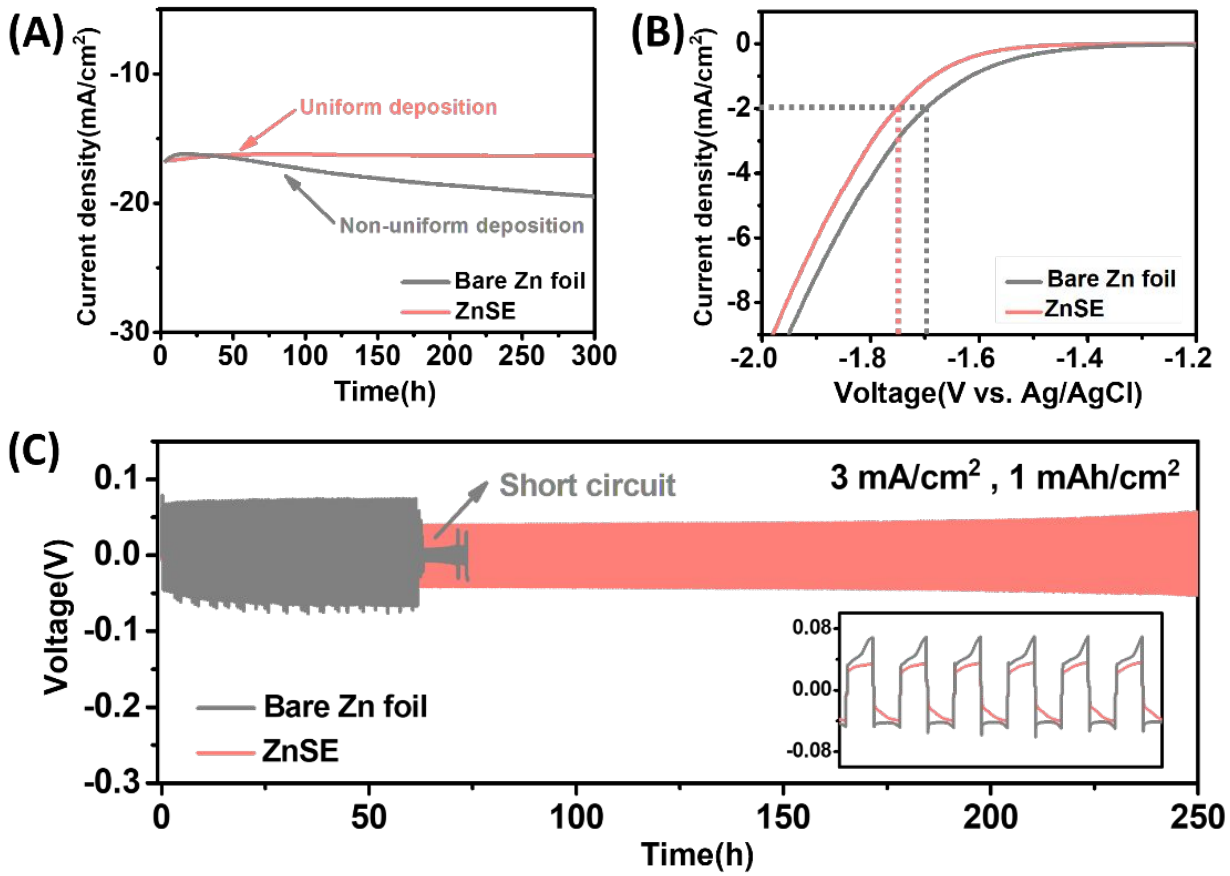

Figure 3. (A) Chronoamperometry curves of the bare Zn foil and ZnSE at a voltage of −150 mV. (B) LSV curves of the bare Zn foil and ZnSE. (C) Voltage profile of the symmetric Zn||Zn cells at the current density of 3 mA/cm^2 and the capacity of 1 mAh/cm^2 for the bare Zn foil and ZnSE.

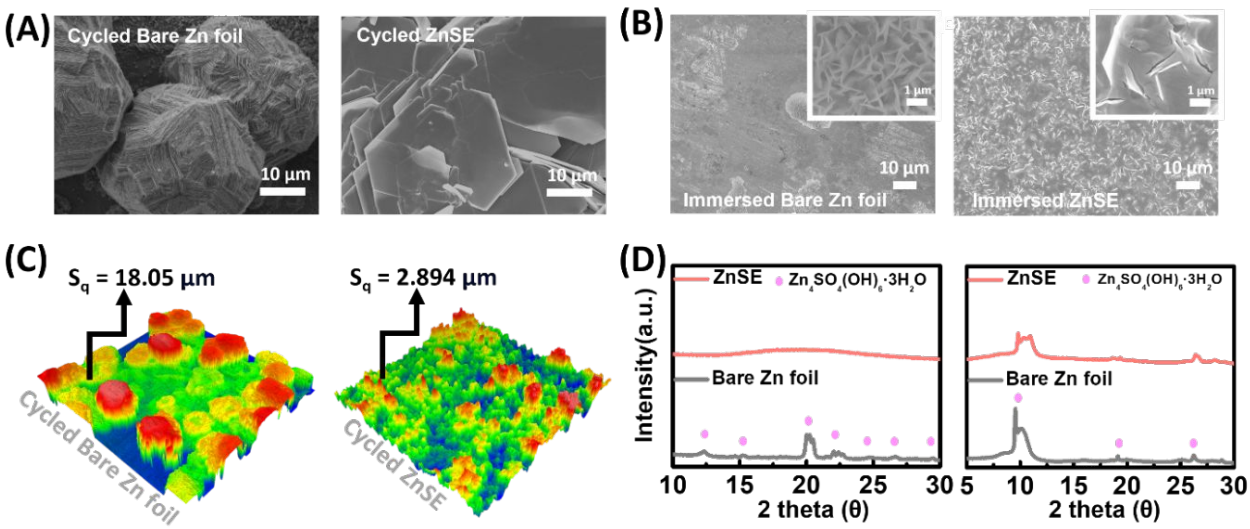

Figure 4. (A) SEM images of the bare Zn foil and ZnSE after the electrochemical dendrite test. (B) SEM images of the bare Zn foil and ZnSE after the by-product test. (C) CSI profiler images of the bare Zn foil and ZnSE after the electrochemical dendrite test. (D) XRD patterns of the bare Zn foil and ZnSE: after (Left) the electrochemical dendrite test and (Right) the by-product test.

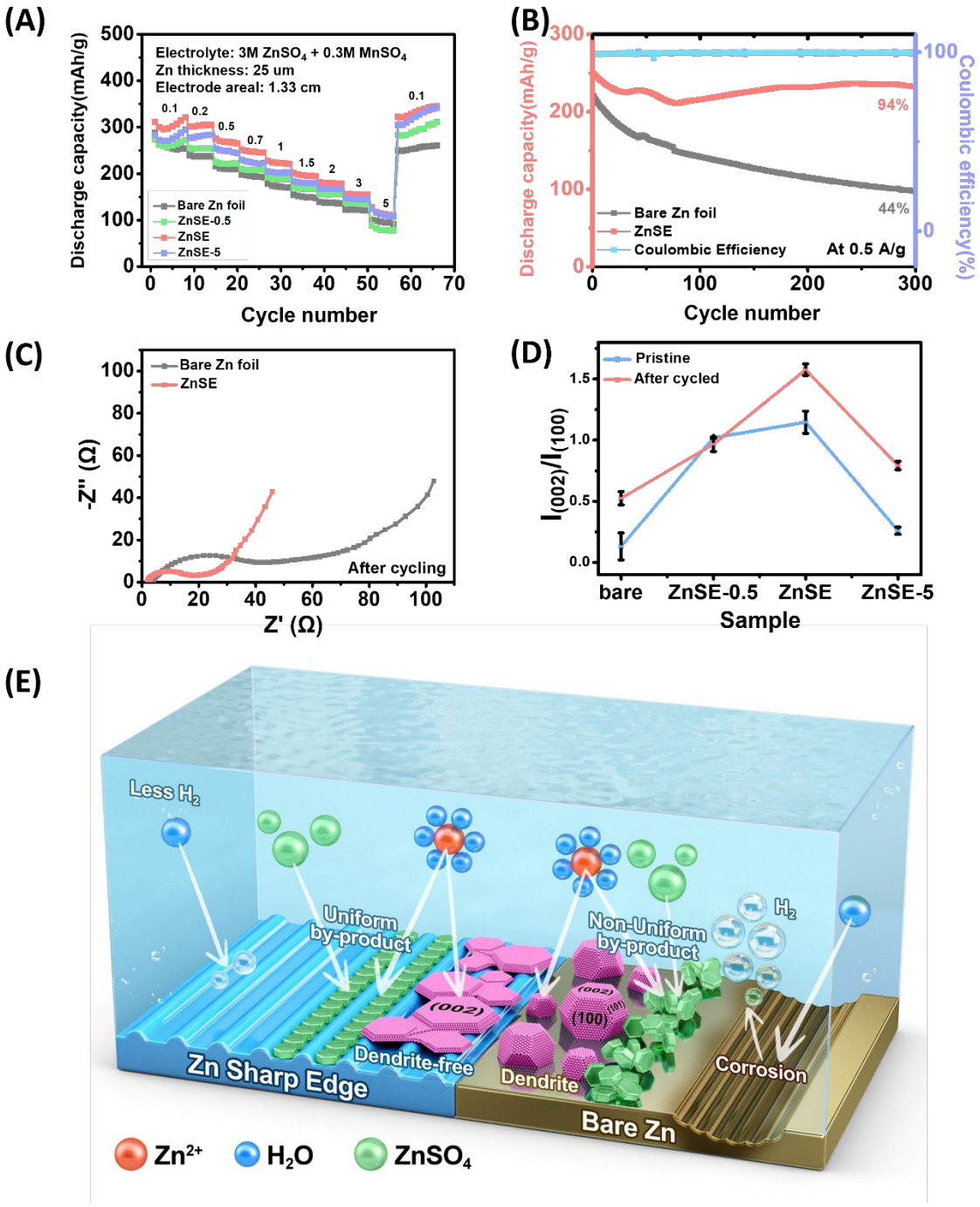

Figure 5. (A) Rate performance of the bare Zn foil, ZnSE-0.5, ZnSE, and ZnSE-5 at the current densities of 0.1–5 A/g. (B) Cycling performance and Coulombic efficiency of the bare Zn foil and ZnSE at the current density of 0.5 A/g. (C) Electrochemical impedance spectra of the bare Zn foil and ZnSE. (D) Peak intensity ratios ($I_{(002)}$ /$I_{(100)}$) of the bare Zn foil and ZnSE. (E) Overall schematic illustration of ZnSE (dendrite-free surface, reduced hydrogen generation, and corrosion resistance)

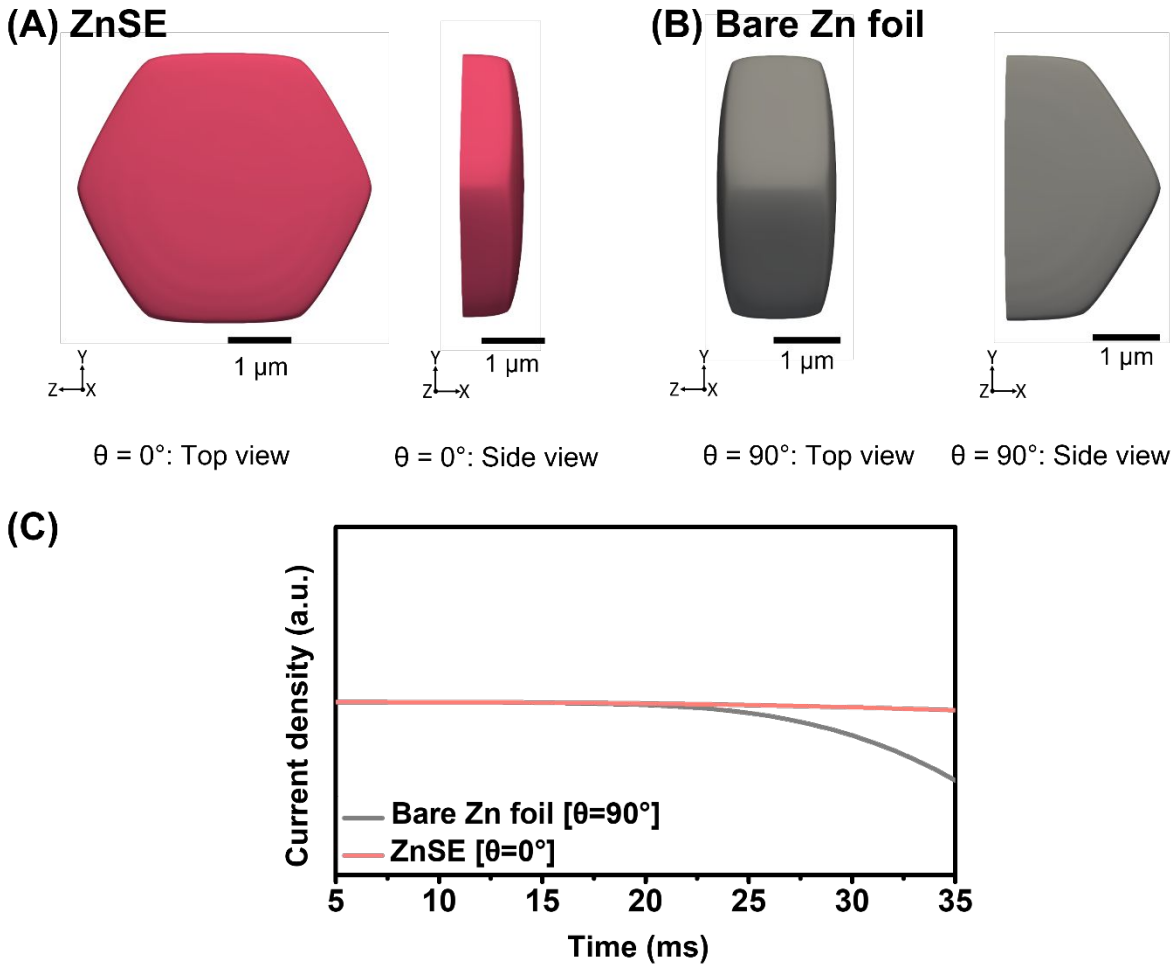

Figure 6. 3D phase-field simulations for Zn deposition microstructure. (A) [002] direction is parallel to X-axis. (B) [002] direction is normal to X-axis. The figures represent the iso-surface of φ at 0.5. (C) Current density developed for two orientations $\theta = 90°$ for bare Zn foil and $\theta = 0°$ for ZnSE.

References

1. M. Huang, X. Wang, X. Liu and L. Mai, *Adv. Mater.*, 2022, **34**, 2105611.
2. N. Nitta, F. Wu, J. T. Lee and G. Yushin, *Mater. Today*, 2015, **18**, 252-264.
3. B. Scrosati and J. Garche, *J. Power Sources*, 2010, **195**, 2419-2430.
4. G. Fang, J. Zhou, A. Pan and S. Liang, *ACS Energy Lett.*, 2018, **3**, 2480-2501.
5. Y. Li, J. Fu, C. Zhong, T. Wu, Z. Chen, W. Hu, K. Amine and J. Lu, *Adv. Energy Mater.*, 2019, **9**, 1802605.
6. J. Ming, J. Guo, C. Xia, W. Wang and H. N. Alshareef, *Mater. Sci. Eng.: R: Rep.*, 2019, **135**, 58-84.
7. W. Xu, K. Zhao, W. Huo, Y. Wang, G. Yao, X. Gu, H. Cheng, L. Mai, C. Hu and X. Wang, *Nano Energy*, 2019, **62**, 275-281.
8. T. Zhang, Y. Tang, S. Guo, X. Cao, A. Pan, G. Fang, J. Zhou and S. Liang, *Energy Environ. Sci.*, 2020, **13**, 4625-4665.
9. M. Wang, X. Zheng, X. Zhang, D. Chao, S.-Z. Qiao, H. N. Alshareef, Y. Cui and W. Chen, *Adv. Energy Mater.*, 2021, **11**, 2002904.
10. W. Lu, C. Xie, H. Zhang and X. Li, *ChemSusChem*, 2018, **11**, 3996-4006.
11. K. E. K. Sun, T. K. A. Hoang, T. N. L. Doan, Y. Yu, X. Zhu, Y. Tian and P. Chen, *ACS Appl. Mater. Interfaces.*, 2017, **9**, 9681-9687.
12. A. Bayaguud, Y. Fu and C. Zhu, *J. Energy Chem.*, 2022, **64**, 246-262.
13. N. Guo, W. Huo, X. Dong, Z. Sun, Y. Lu, X. Wu, L. Dai, L. Wang, H. Lin, H. Liu, H. Liang, Z. He and Q. Zhang, *Small Methods*, 2022, **6**, 2200597.
14. M. Zhou, S. Guo, J. Li, X. Luo, Z. Liu, T. Zhang, X. Cao, M. Long, B. Lu, A. Pan, G. Fang, J. Zhou and S. Liang, *Adv. Mater.*, 2021, **33**, 2100187.
15. Y. Lin, Z. Mai, H. Liang, Y. Li, G. Yang and C. Wang, *Energy Environ. Sci.*, 2023, **16**, 687-697.

16. J. Feng, X. Li, X. Cui, H. Zhao, K. Xi and S. Ding, *Adv. Energy Mater.*, 2023, **13**, 2204092.
17. H. Lu, Q. Jin, X. Jiang, Z.-M. Dang, D. Zhang and Y. Jin, *Small*, 2022, **18**, 2200131.
18. X. Jia, C. Liu, Z. G. Neale, J. Yang and G. Cao, *Chem. Rev.*, 2020, **120**, 7795-7866.
19. W. Guo, Y. Zhang, X. Tong, X. Wang, L. Zhang, X. Xia and J. Tu, *Mater. Today Energy*, 2021, **20**, 100675.
20. Y. Liu, T. Guo, Q. Liu, F. Xiong, M. Huang, Y. An, J. Wang, Q. An, C. Liu and L. Mai, *Mater. Today Energy*, 2022, **28**, 101056.
21. H. Zhang, Y. Zhong, J. Li, Y. Liao, J. Zeng, Y. Shen, L. Yuan, Z. Li and Y. Huang, *Adv. Energy Mater.*, 2023, **13**, 2203254.
22. J. Zhang, W. Huang, L. Li, C. Chang, K. Yang, L. Gao and X. Pu, *Adv. Mater.*, 2023, **35**, 2300073.
23. T.-T. Su, K. Wang, B.-Y. Chi, W.-F. Ren and R.-C. Sun, *EcoMat*, 2022, **4**, e12219.
24. J. Wang, B. Zhang, Z. Cai, R. Zhan, W. Wang, L. Fu, M. Wan, R. Xiao, Y. Ou, L. Wang, J. Jiang, Z. W. Seh, H. Li and Y. Sun, *Sci. Bull.*, 2022, **67**, 716-724.
25. R. Yuksel, O. Buyukcakir, W. K. Seong and R. S. Ruoff, *Adv. Energy Mater.*, 2020, **10**, 1904215.
26. H. Tian, Z. Li, G. Feng, Z. Yang, D. Fox, M. Wang, H. Zhou, L. Zhai, A. Kushima, Y. Du, Z. Feng, X. Shan and Y. Yang, *Nat. Commun.*, 2021, **12**, 237.
27. G. Lin, X. Zhou, L. Liu, D. Huang, H. Li, X. Cui and J. Liu, *RSC Adv.*, 2022, 12, 25054-25059.
28. Y. Chen, Z. Deng, Y. Sun, Y. Li, H. Zhang, G. Li, H. Zeng and X. Wang, *Nano Lett.*, 2024, 16, 96.
29. Z. Zhao, J. Lai, D. T. Ho, Y. Lei, J. Yin, L. Chen, U. Schwingenschlögl and H. N. Alshareef, *ACS Energy Lett.*, 2023, 8, 608-618.

30. L. Su, F. Lu, Y. Li, X. Li, L. Chen, Y. Gao, L. Zheng and X. Gao, ChemSusChem, 2023, 16, e202300285.
31. L. Cao, D. Li, E. Hu, J. Xu, T. Deng, L. Ma, Y. Wang, X.-Q. Yang and C. Wang, *J. Am. Chem. Soc.,* 2020, 142, 21404-21409.
32. X. Li, H. Wang, X. Sun, J. Li and Y.-N. Liu, *ACS Appl. Energy Mater.*, 2021, 4, 12718-12727.
33. W. Wang, G. Huang, Y. Wang, Z. Cao, L. Cavallo, M. N. Hedhili and H. N. Alshareef, *Adv. Energy Mater.*, 2022, **12**, 2102797.
34. Y. Zeng, X. Zhang, R. Qin, X. Liu, P. Fang, D. Zheng, Y. Tong and X. Lu, *Adv. Mater.*, 2019, **31**, 1903675.
35. V. Jabbari, T. Foroozan and R. Shahbazian-Yassar, *Adv. Energy Mater.*, 2021, **2**, 2000082.
36. T. E. Graedel, *J. Electrochem.*, 1989, **136**, 193C.
37. A. Roy and P.-R. Cha, *J. Appl. Phys.*, 2020, **128**.
38. A. Roy, M.-G. Cho and P.-R. Cha, *J. Appl. Phys.*, 2022, 131.
39. A. Roy and P.-R. Cha, *Mater. Trans.*, 2022, **63**, 1662-1669.
40. D. Tourret and A. Karma, *Acta Mater.*, 2015, **82**, 64-83.
41. P. C. Hohenberg and B. I. Halperin, *REV MOD PHYS.*, 1977, **49**, 435-479.
42. S. L. Wang, R. F. Sekerka, A. A. Wheeler, B. T. Murray, S. R. Coriell, R. J. Braun and G. B. McFadden, *PHYSICA D.*, 1993, **69**, 189-200.
43. S. G. Kim, W. T. Kim and T. Suzuki, *PRE*, 1999, **60**, 7186-7197.
44. H. M. Singer, I. Singer-Loginova, J. H. Bilgram and G. Amberg, *J. Cryst. Growth*, 2006, **296**, 58-68.
45. V. Yurkiv, T. Foroozan, A. Ramasubramanian, M. Ragone, R. Shahbazian-Yassar and F. Mashayek, *J. Electrochem. Soc.*, 2020, **167**, 060503.

46. Z. Hong, Z. Ahmad and V. Viswanathan, *ACS Energy Lett.*, 2020, **5**, 2466-2474.

47. B. Böttger, J. Eiken and I. Steinbach, *Acta Mater.*, 2006, **54**, 2697-2704.

48. T. Takaki, T. Shimokawabe, M. Ohno, A. Yamanaka and T. Aoki, *J. Cryst. Growth*, 2013, **382**, 21-25.